ROYAL SOCIETY OF CHEMISTRY

PAPER

Check for updates

Stabilizing cubic γ-Ga$_2$O$_3$:Cr^{3+} spinel nanocrystals by size confinement into mesoporous silica nanoreactor channels†

Michele Crozzolin, [a] Camilla Belloni, [a] Jian Xu, [bc] Takayuki Nakanishi, [d] Jumpei Ueda,[e] Setsuhisa Tanabe, [c] Federico Dallo,[f] Eleonora Balliana, [g] Asia Saorin, [a] Flavio Rizzolio, [ah] Davide Cristofori, [a] Pietro Riello, [a] Alvise Benedetti [a] and Michele Back [*a]

In recent years, Cr^{3+}-activated phosphors have been attracting a lot of interest due to their unique optical features that can be exploited for applications ranging from lasers to optical thermometry, near-infrared (NIR) emitting phosphors for bioimaging and NIR-LEDs, to name a few. Despite the interesting optical properties shown by Cr^{3+}-doped Ga$_2$O$_3$, investigations are limited only to β-Ga$_2$O$_3$ and α-Ga$_2$O$_3$ polymorphs. Using mesoporous silica particles with different pore sizes between 3 nm and 22 nm as nanoreactors, cubic γ-Ga$_2$O$_3$:Cr^{3+} spinel nanocrystals (NCs) are stabilized through confinement into the mesopores as confirmed by HR-TEM, XRPD and the photoluminescence spectral shape. A detailed spectroscopic investigation in the temperature range between 16 to 500 K allowed extrapolating the fundamental parameters in the framework of the Tanabe−Sugano diagram and comparing the values for Cr^{3+} in γ-Ga$_2$O$_3$ with the α- and β-phases. In addition, due to the confinement of the NCs into the silica structure, the phase transition to the β-phase, conventionally occurring at about 700 °C, is hindered up to 1000 °C, improving the stability of the γ-Ga$_2$O$_3$ phase.

Introduction

Since the discovery of the ruby laser by Maiman,[1] Cr^{3+}-doped crystals have been among the most investigated transition metal ion doped phosphors. The flexibility of the optical properties of Cr^{3+} ions, arising from the possibility to control the relative energy level position of the low lying ^{4}T$_2$ and

^{a} *Department of Molecular Sciences and Nanosystems, Ca' Foscari University of Venice, Via Torino 155, 30172, Mestre – Venezia, Italy.*
E-mail: michele.back@unive.it

^{b} *International Center for Young Scientists (ICYS), National Institute of Materials Science (NIMS), Tsukuba, Ibaraki 305-0044, Japan*

^{c} *Graduate School of Global Environmental Studies, Kyoto University, Yoshida nihonmatsu-cho, Sakyo-ku, Kyoto 606-8501, Japan*

^{d} *Advanced Phosphor Group, National Institute of Materials Science (NIMS), Tsukuba, Ibaraki 305-0044, Japan*

^{e} *Graduate School of Advanced Science and Technology, Japan Advanced Institute of Science and Technology (JAIST), 1-1 Asahidai, Nomi, Ishikawa, 923-1292, Japan*

^{f} *Institute of Polar Sciences – National Research Council (ISP-CNR), Via Torino 155, 30172, Venezia-Mestre, Venice, Italy*

^{g} *Department of Environmental Sciences, Informatics, Statistics, Ca' Foscari University of Venice, Scientific Campus – Via Torino 155, 30170 Venezia Mestre, Italy*

^{h} *Pathology Unit, Department of Molecular Biology and Translational Research, Centro di Riferimento Oncologico di Aviano (CRO) IRCCS, via Franco Gallini 2, 33081 Aviano, Italy*

† Electronic supplementary information (ESI) available. See DOI: **https://doi.org/10.1039/d4tc01386g**

Michele Back

Michele Back is a tenure track assistant professor in Chemical Sciences at the Department of Molecular Sciences and Nano-systems, Ca' Foscari University of Venice. He completed his MS in Materials Science in 2013 and PhD in Chemical Sciences in 2017. He then undertook a JSPS postdoctoral fellowship at Kyoto University (2017–2019) with Prof. Setsuhisa Tanabe. He was a research fellow at the Centro di Riferimento Oncologico (CRO) IRCCS, Aviano (2020–2021) and a research scientist at NIMS as a JSPS invitational fellow (2023). The goal of his research is the establishment of structure-luminescence relationships to develop models able to predict optical properties. His current research interests focus on the fundamental aspects and development of luminescent inorganic (nano-)materials for optoelectronic and sensing applications.

This journal is © The Royal Society of Chemistry 2024

J. Mater. Chem. C, 2024, **12**, 10929–10941 | **10929**

^{2}E excited states through the bond lengths and symmetry of the octahedral site of the host, has led to a huge interest in developing new Cr^{3+}-doped phosphors for a wide variety of applications. Demonstration of the potential of Cr^{3+} ions in persistent luminescent materials such as spinel $ZnGa_2O_4$,[2,3] garnets (*e.g.* $Y_5Al_{3-x}Ga_xO_{12}$[4–6]) and perovskite $LaAlO_3$[7] has triggered investigation into their use in biological applications. In addition, Cr^{3+}-activated phosphors were also demonstrated to be particularly promising as luminescent thermometers based on the ratio between the emissions originated from the spin allowed $^4T_2 \rightarrow {}^4A_2$ and the spin forbidden $^2E \rightarrow {}^4A_2$ transitions,[8–12] which were proposed for a wide range of temperatures ranging from the cryogenic ($CaHfO_3$:Cr^{3+}[13]) to high temperatures ($ZnGa_2O_4$:Cr^{3+}[14]). The ability to customize the working temperature range arises from the possibility of modulating the relative energy gap between the $^4T_2$ and ^2E states. This modulation is achieved by adjusting the octahedral site through the selection of specific host compositions and structures.[15] On the other hand, due to the high stability and efficiency of ruby (α-Al_2O_3:Cr^{3+}) when used as a pressure sensor in diamond anvil cell experiments all over the world,[16–18] Cr^{3+}-doped phosphors were also deeply investigated to discover pressure sensors with higher sensitivities.[19–21] More recently, the commercialization of near infrared (NIR) emitting phosphor-converted LEDs based on Cr^{3+}-doped phosphors by Osram, has driven a lot of interest in the development of novel NIR Cr^{3+}-based phosphors characterized by broadband $^4T_2$ emission in weak crystal fields for applications ranging from food and medicine quality monitoring to bioimaging, night vision and plant growth.[22–24] From this perspective, the exploration of novel phosphors activated by Cr^{3+} ions remains highly active.

Gallium oxide (Ga_2O_3) is emerging as one of the most important materials for a variety of technological applications.[24] Ga_2O_3 is a semiconductor capable of adopting various crystallographic structures, with six different polymorphs known: the stable β-phase and five metastable phases α, γ, δ, ε, and κ.[25,26] Among them, β-Ga_2O_3 has been demonstrated to be a promising host for Cr^{3+}-activated phosphors[27–31] and has been investigated for lasing,[28] optical thermometry[15] and pc-NIR LEDs.[32] A detailed spectroscopic investigation on Cr^{3+} ions in the rhombohedral α-Ga_2O_3 phase was recently reported, showing a stronger crystal field with respect to β-Ga_2O_3.[15] In addition, a corundum-type α-Ga_2O_3:Cr^{3+} system was also proposed as a pressure sensor.[33] Al_2O_3–Ga_2O_3 and Sc_2O_3–Ga_2O_3 solid solutions were also deeply investigated as promising hosts for Cr^{3+} ions.[34,35]

The crystalline structure of the γ-Ga_2O_3 polymorph has been widely investigated and debated due to the complicated defect $Fd\bar{3}m$ spinel structure.[36–40] γ-Ga_2O_3 stabilization was also proved in glassy hosts[41] showing photocatalytic and catalytic activity.[42–44] The defects present in the γ-Ga_2O_3 spinel structure were exploited to develop size-tuneable luminescent nanocrystals[45] and white-light-emitting nanophosphors when coupled through energy transfer with orange-red emitting organic dyes.[46] Despite the interest in Ga_2O_3 polymorphs as hosts for luminescent centres, a detailed investigation on the Cr^{3+} optical properties in cubic γ-Ga_2O_3 is still missing.

In this study, we investigate the stabilization of Cr^{3+}-doped γ-Ga_2O_3 nanocrystals (NCs) by taking advantage of the size effect in mesoporous silica particles (MSPs) of different pore sizes. The effects of the size and temperature were investigated by means of a series of physical chemical investigation using XRPD, SEM/HR-TEM, N_2 physisorption and TG–DSC analyses. In addition, the photoluminescence (PL) spectral analysis of Cr^{3+} in the Ga_2O_3 NCs allowed a detailed spectroscopic investigation to probe the crystalline structure. The HR-TEM analysis confirmed the stabilization of the cubic γ-Ga_2O_3 spinel structure. Moreover, a detailed investigation of the photoluminescence (PL) and PL excitation (PLE) spectral analysis and the temperature dependence of the PL spectra led to a comparison of the spectroscopic feature of Cr^{3+} with respect to the β- and α-Ga_2O_3 polymorphs and to investigations into the effect of the crystal on the $3d^3$ electrons of Cr^{3+} in terms of a Tanabe–Sugano diagram and configurational coordinate diagram.

Results and discussion

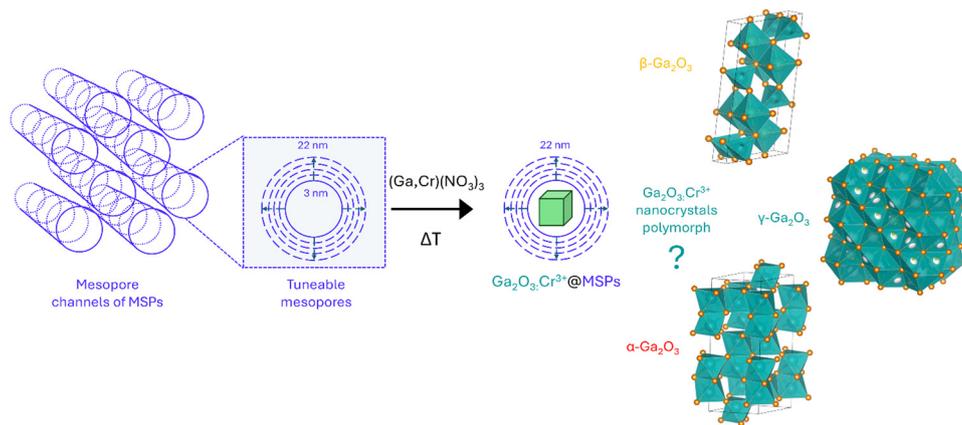### Stabilizing γ-Ga_2O_3 polymorphs by size: MSP pore effect

The most common Ga_2O_3 polymorphs, α, β and γ, exhibit distinct differences in crystal structures and coordination polyhedra with a direct influence on their stability and synthetic methods. The trigonal α-Ga_2O_3 (space group $R\bar{3}c$) is characterized by a corundum structure with only octahedral GaO_6 sites, while β-phase by a monoclinic structure (space group $C2/m$) with mixed coordination of octahedral GaO_6 and tetrahedral GaO_4 sites with a ratio $1:1$ and the cubic γ-phase (space group $Fd\bar{3}mZ$) by a defective spinel structure with both octahedral and tetrahedral sites characterized by a high degree of disorder.[36–40] The unit cell volume increases by moving from the compact β-Ga_2O_3 (~ 209 $Å^3$) to α-Ga_2O_3 (~ 289 $Å^3$) and finally to the defective γ-Ga_2O_3 (~ 559 $Å^3$).

With the aim of investigating suitable sizes to stabilize the cubic γ-Ga_2O_3 phase, mesoporous silica particles with different mesopores were firstly synthesized as nanoreactors and subsequently the Cr^{3+}-doped Ga_2O_3 nanocrystals were grown by means of an impregnation procedure followed by thermal treatment (Scheme 1).

MSPs characterized by five different average pore sizes were firstly prepared as shown in Fig. 1a (labelled as MSP_3.1, MSP_4.2, MSP_7.5, MSP_13.5 and MSP_22.4).

Different synthetic procedures were employed to obtain access to MSPs characterized by different pore sizes. Spherical MSNs, with an average pore size of 3.1 nm (Fig. 1b), were obtained following the procedure proposed by Quiao et al.[47] Spherical MCM-41 MSNs characterized by a pore size of 4.2 nm were prepared using *n*-hexane as the swelling agent (Fig. 1c). SBA-15 with average pores of 7.5 nm were synthesized using an aging process in an autoclave at 100 °C for 24 hours without the use of a swelling agent, while SBA-15 characterized by average

10930 | J. Mater. Chem. C, 2024, 12, 10929–10941

This journal is © The Royal Society of Chemistry 2024

Scheme 1 Sketch of the synthetic procedure for the synthesis of Ga_2O_3:Cr^{3+} nanocrystals with tunable size inside the mesopores of MSPs by means of a wet impregnation strategy followed by thermal treatment and the most common Ga_2O_3 polymorphs that could be stabilized.
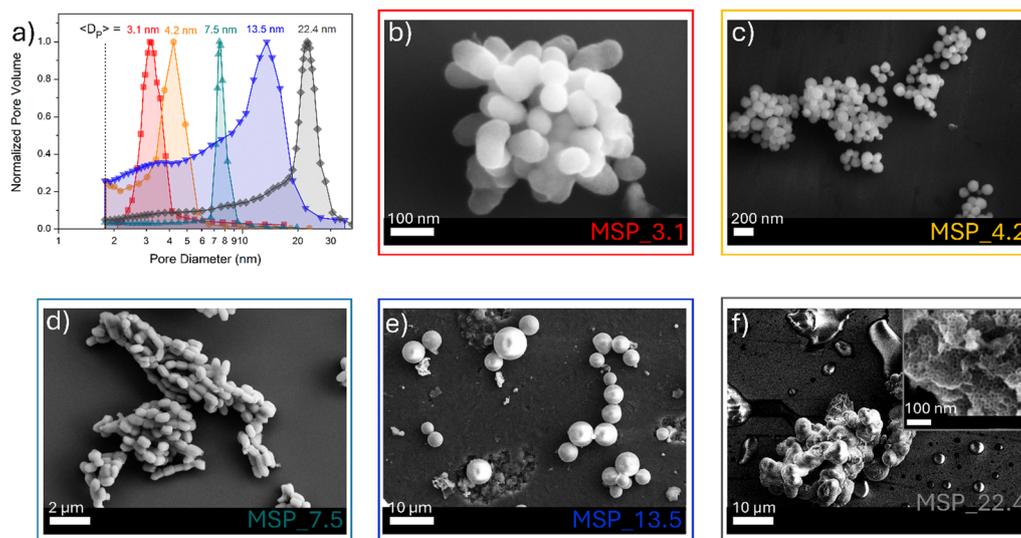
Fig. 1 (a) BJH pore size distribution of MSPs and (b)–(f) the corresponding representative FE-SEM images.

pore sizes of 13.5 and 22.4 nm were prepared by using trimethylbenzene at different TMB/Pluronic P123 ratios as the swelling agent. The SBA-15 are characterized by typical hexagonal arranged pore structure morphology (Fig. 1d and Fig. S1a and b, ESI†). The conventional tubular shape is lost, and micrometer globular particles are stabilized when a TMB/Pluronic P123 ratio of 0.3 : 1 is employed (Fig. 1e and Fig. S1c and d, ESI†). Finally, mesocellular foam with average pore sizes of 22.4 nm were obtained for a TMB/Pluronic P123 ratio of 0.5 : 1 (Fig. 1f and Fig. S1e and f, ESI†). The shape evolution is driven by the TMB/Pluronic P123 ratio due to the effect of TMB on the surfactant packing parameter.[48] TMB can be easily dissolved into the PPO core of P123 micelles increasing the volume of the hydrophobic part.[49] This change directly influences the micelle shape, described through the geometric model introduced by Israelachvili[50] by the packing factor $P = V/(a_0 l)$, where V is the total volume of the hydrophobic surfactant chain, a_0 the effective hydrophilic headgroup size and l is

the kinetic surfactant tail length. When the TMB/Pluronic P123 ratio is high ($P > 1$), the need to decrease the micelle surface-to-volume ratio leads to micellar aggregates with reverse curvature being formed[51] and a consequent change in the mesoporous silica structure to mesocellular foam is triggered.

The N_2 physisorption analysis allows estimating the surface area using the BET technique (Table S1, ESI†) while the pore size distributions and pore volume of the different MSPs were determined using the BJH method (Fig. 1a and Table S1, ESI†). The N_2 physisorption hysteresis curves of the MSP samples are shown in Fig. S2 (ESI†).

Subsequently, the MSPs were impregnated with Ga/Cr nitrate precursors using a wet impregnation method by fixing the Ga : Cr ratio to obtain a 0.5 at% doping of the Ga sites in the final target product ($Ga_{1.99}Cr_{0.01}O_3$). After that, the system was thermally treated at 900 °C for 2 hours.

At this stage of the preparation, the XRPD pattern analysis of the samples, shown in Fig. 2a, independently from the pore
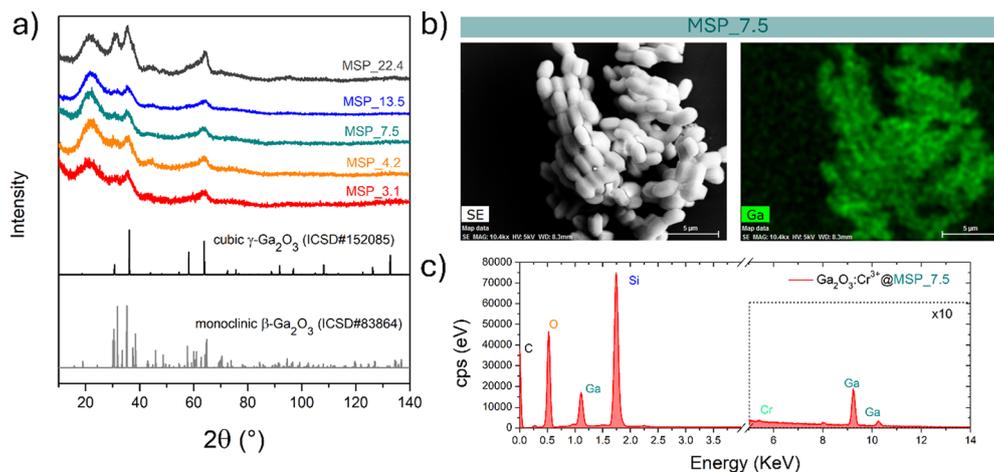
This journal is © The Royal Society of Chemistry 2024

J. Mater. Chem. C, 2024, **12**, 10929–10941 | **10931**

Fig. 2 (a) XRPD patterns of the samples with increasing pore size of the mesopores of the MSPs where the Ga_2O_3 NCs were grown. (b) Representative secondary electron-SEM image and corresponding EDX elemental map of Ga and (c) EDX spectrum of the Ga_2O_3:Cr^{3+}@MSP_7.5 sample.

size, show a pattern similar to that of the γ-Ga_2O_3 spinel reference, suggesting stabilization of the higher symmetric cubic structure. However, the broadening of the diffraction peaks due to the small crystallites and the amorphous contribution of the MSPs make the assignment not unambiguous.

The effectiveness of the impregnation method is demonstrated by the elemental map of Ga inside the MSPs by means of EDX analysis. As shown in Fig. 2b on the Ga_2O_3:Cr^{3+}@MSP_7.5 sample, as an example, Ga is homogeneously distributed inside the MSPs. In addition, the EDX spectrum allows us to confirm the Si, Ga and Cr elements are present in the particles. The elemental maps of Ga, Si and O confirmed the effectiveness of the impregnation irrespective to the pore size as evidenced for instance by the elemental maps for Ga_2O_3@MSP_4.2, Ga_2O_3@MSP_7.5 and Ga_2O_3@MSP_13.5 reported in Fig. S3–S5 (ESI†).

To shed light on the phase assignment, Cr^{3+} ions can be used as a structural probe. Indeed, the strong effect of the environment on the optical properties of the $3d^3$ electrons of Cr^{3+} can be used to probe the stabilized polymorphs. In this way, bulk monoclinic β-Ga_2O_3:Cr^{3+} was prepared as a reference. The photoluminescence (PL) spectra of Ga_2O_3:Cr^{3+} nanocrystals in Fig. 3a reveal an unexpected behavior showing the stabilization of the γ-Ga_2O_3 spinel phase for NCs of 7.5 and 13.5 nm, confirming the XRPD analysis, while at smaller sizes the stable monoclinic β-phase is detected. The PL spectrum of the 22.4 nm sample shows the spectral feature of both the β-phase and γ-phase, suggesting a mixture of the polymorphs. Irrespective of the stabilized phase, the integrated PL area increases linearly with the size of the NCs (Fig. 3b) evidencing a major role played by the size on the quenching behavior.

Fig. 3c summarizes the results of the Ga_2O_3 polymorph stabilization into the mesoporous channels with different size ranges. The stabilization of the cubic γ-Ga_2O_3 phase can be explain by considering the complex interplay between surface energy and bulk thermodynamic stability along with synthesis conditions. The order of phase stability (based on the formation free energy) for the Ga_2O_3 polymorphs is $\beta > \kappa > \alpha > \delta > \gamma$.[52,53] However, at the nanoscale, the surface to volume ratio increases leading the surface energy playing a significant role in the total energy. On the other hand, high-symmetry phases tend to have lower surface energy making the γ-phase more favorable at small sizes. The stabilization of higher symmetric structures with the decreasing of the size was already demonstrated for many partially covalent compounds such as CdSe,[54,55] ZrO_2,[56] YPO_4, $BaTiO_3$, Al_2O_3, Fe_2O_3, $PbTiO_3$, $PbZrO_3$, and $Bi_2CaSr_2Cu_2O_8$,[57] to name a few. With reduction in particle size, a unit cell expansion up to phase transition was demonstrated for these materials, showing an effect similar to the application of a negative pressure.[57]

The stabilization of the β-Ga_2O_3 phase for a size smaller than 4.2 nm confirms the results reported by Fang *et al.*[58] and it could be explained considering that the kinetic barriers that need to be overcome to stabilize different polymorphs can be strongly altered by stress and strain, promoting or hindering the stabilization of metastable polymorphs. The same effect of size dependence stabilization of the γ- and β-phase was also recently demonstrated for ultrathin Ga_2O_3 nanowires by Wang *et al.*,[59] suggesting that positive or negative strains could inhibit the phase transition to the γ-phase at very small sizes. For sizes larger than about 22 nm, the β-Ga_2O_3 polymorph is again the more thermodynamically favored.

The sample at 7.5 nm was selected as representative of the cubic γ-Ga_2O_3:Cr^{3+}. As evidenced in Fig. S2 (ESI†) and Fig. 1a, the MSP_7.5 sample is characterized by a type H1 hysteresis loop (IUPAC[60]) typical of the SBA-15 and a narrow pore size distribution. The XRPD patterns at low angles of the bare MSP_7.5 show the characteristic reflections of the (100), (110) and (200) planes of the *p6mm* hexagonally arranged cylindrical pores[61,62] (Fig. 4a). The well resolved peaks indicate the high degree of hexagonal mesoscopic organization. The intense (100) peak reflects a *d* spacing of 94 Å, corresponding to a large unit cell parameter $a = 10.9$ nm. After the Ga_2O_3 NCs growth into the MSP channels at 900 °C, the *p6mm* morphology is

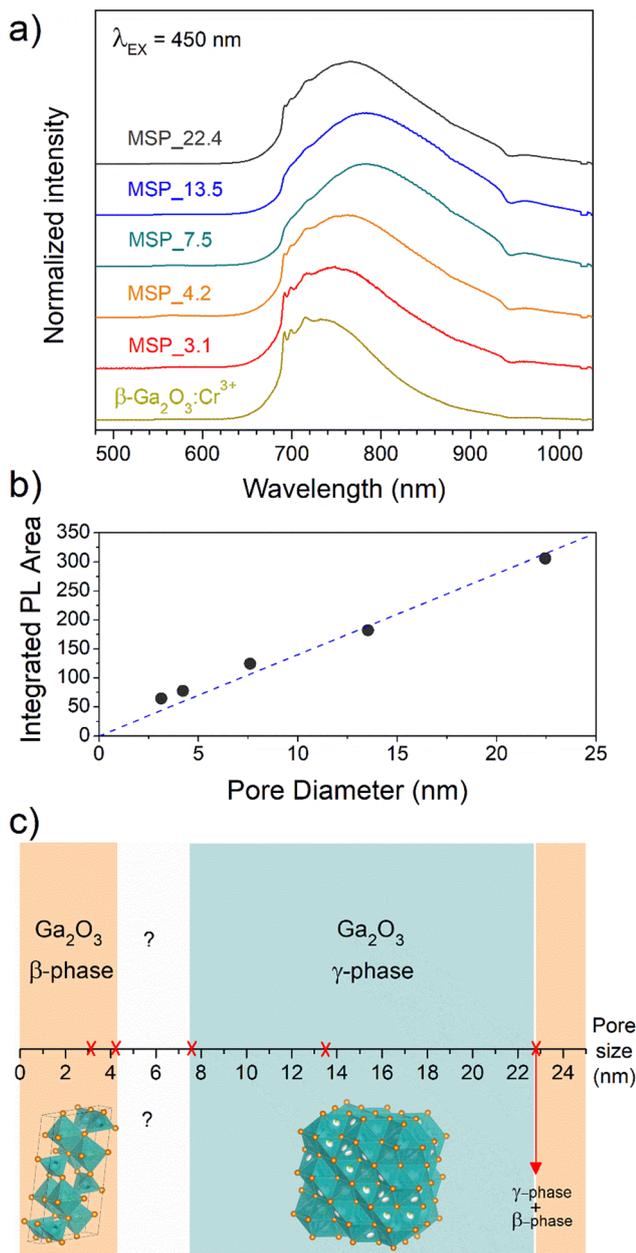**10932** | *J. Mater. Chem. C*, 2024, **12**, 10929–10941

This journal is © The Royal Society of Chemistry 2024

Fig. 3 (a) PL spectra of Cr^{3+} in Ga$_2$O$_3$ NCs grown in mesopores of different size, (b) integrated PL area as a function of the pore size and (c) diagram of the stabilized Ga$_2$O$_3$ polymorph *versus* pore size.

preserved but the peaks appear at larger 2θ values, with $d_{(100)} = 98$ Å and $a = 9.8$ nm. Fig. 4b shows the XRPD at higher angles of the bare SBA-15 MSPs, the SBA-15 MSPs filled with the Ga$_2$O$_3$:Cr^{3+} nanocrystals after the thermal treatment at 900 °C and the Ga$_2$O$_3$:Cr^{3+} nanocrystals after the MSP etching by NaOH. Comparison with the Ga$_2$O$_3$ polymorph references evidences the stabilization of the cubic γ-phase. In addition, the theoretical amount of Cr doping was confirmed using ICP-OES analysis. The estimated Ga:Cr = 28.62:0.18 shows a doping content of 0.6 at%, in good agreement with the theoretical value of 0.5% of the Ga sites (Ga$_{1.99}$Cr$_{0.01}$O$_3$).

The TEM image of the mesoporous silica MSP_7.5 (Fig. 4c) shows the well-organized mesopores, as expected by the pore distribution (Fig. 1a) and the XRPD at low angles (Fig. 4a). Fig. 4d and e and Fig. S6 (ESI†) show the HR-TEM images of the Ga$_2$O$_3$ NCs grown into the mesopores of the MSP_7.5 after the etching process. The HR-TEM analysis (Fig. 4e) provides additional evidence of the stabilization of the cubic γ-Ga$_2$O$_3$ polymorph. The images confirm the high crystalline nature of the Ga$_2$O$_3$ NCs and the investigation of the *d*-spacing of the families of planes evidenced in the HR-TEM images are unambiguously assigned to the (311), (222), and (422) crystal planes, characteristic of the cubic γ-Ga$_2$O$_3$ polymorph (Table S2, ESI†). The very narrow size distribution of the NCs estimated by TEM (numerical distribution, $N(D)dD$) shows a mean value of 6.9 ± 1.0 nm in good agreement with the pore size distribution obtained using the BJH method (volumetric distribution, $V(D)dD$ also in this case vary narrow) confirming the stabilization of the γ-Ga$_2$O$_3$ NCs inside the pores of the MSP_7.5 (Fig. 4f). Assuming that the average pore length L is independent of the pore diameter, the two distributions are correlated by $V(D)dD = N(D)\frac{\pi D^2}{4} L dD$,[63] and the $N(D)$ obtained by TEM is compared with $V(D)/D^2$ obtained by BJH.

It is worth noting that if the silica is etched from the Ga$_2$O$_3$@MSP system without the use of an ultrasonic bath, this nanocasting method leads to a mesoporous γ-Ga$_2$O$_3$ replica of the SBA-15 (see Fig. S7, ESI†) with potential applications as a support for nanocatalysts or directly as a mesoporous catalyst itself.[42,43]
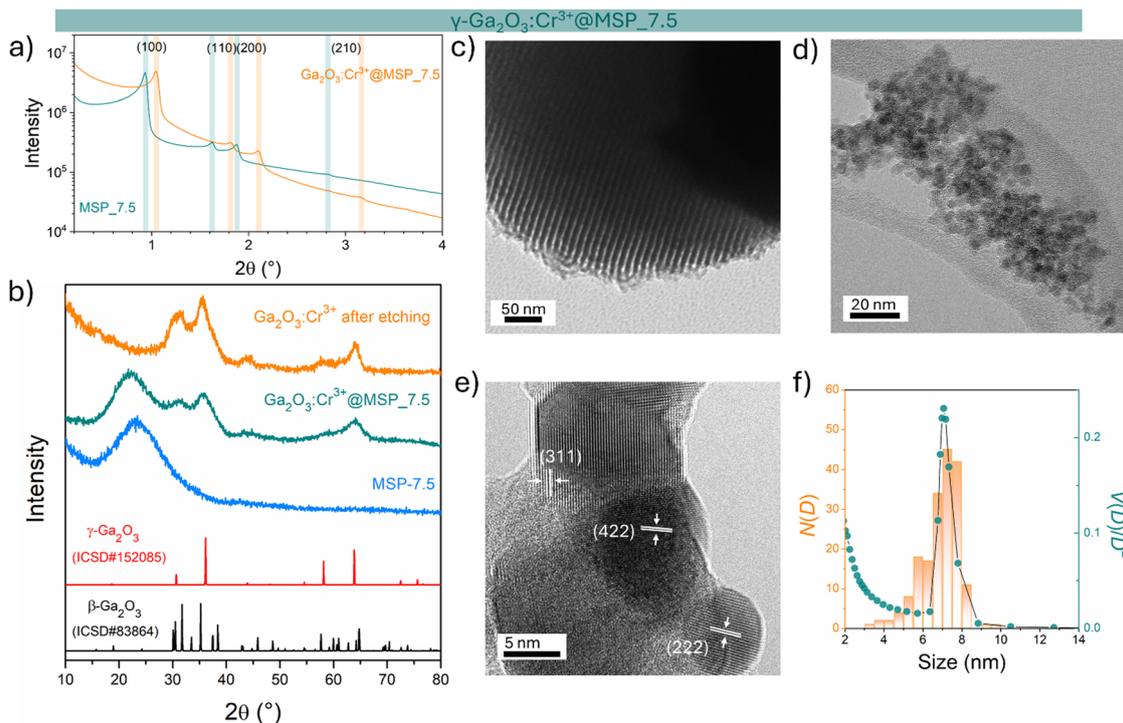
The cubic γ-Ga$_2$O$_3$ spinel phase is well known to undergo a phase transition to the β-phase at high temperature.[39,64,65] In order to investigate the effect of the silica structure on the phase stability, the effect of thermal treatment at 1000 °C was studied by comparing the results of TG–DSC analysis with the XRPD and the PL spectral shape after the annealing.

The TG–DSC analysis on the γ-Ga$_2$O$_3$:Cr^{3+}@MSP_7.5 system (Fig. S8, ESI†) evidences the lack of phase transitions in the range explored, up to 1000 °C and the thermal stability of the system. This is also confirmed by the XRPD analysis and the comparison of the PL spectra of the sample after the treatment. As clearly visible in Fig. 5a and b, the γ-phase is kept, suggesting that the phase transformation from γ to β recorded by Castro-Fernandez *et al.*[39] at 550–750 °C for nanocrystals of about 2.5 nm is influenced by the size. Moreover, the silica structure can also play an important role. However, the stability of the γ-Ga$_2$O$_3$ spinel structure up to 1000 °C could be very important for instance for applications in high temperature catalysis.

Spectroscopic investigation and thermal stability of γ-Ga$_2$O$_3$:Cr^{3+} spinel nanocrystals

In order to investigate the effect of the local crystal site on the 3d^3 electrons of Cr^{3+}, spectroscopic investigation is performed. Fig. 6a shows the PL and PLE spectra of Cr^{3+} in the cubic γ-Ga$_2$O$_3$ spinel NCs. The PL spectrum is characterized by

This journal is © The Royal Society of Chemistry 2024

J. Mater. Chem. C, 2024, **12**, 10929–10941 | **10933**

Fig. 4 Stabilization of γ-Ga$_2$O$_3$ NCs into MSP_7.5: structural and morphological analysis. (a) XRPD at low angles of the bare MSP_7.5 and the γ-Ga$_2$O$_3$@MSP_7.5 sample. (b) Comparison of the XRPD patterns at higher angles of the bare MSP_7.5, Ga$_2$O$_3$:Cr^{3+}@MSP_7.5 annealed at 900 °C and the Ga$_2$O$_3$:Cr^{3+} NCs etched from the MSP_7.5. TEM images of (c) MSP_7.5 and (d) etched Ga$_2$O$_3$ NCs. (e) HR-TEM of the etched Ga$_2$O$_3$ NCs together with the d-spacing and (*hkl*) assignment of the crystalline planes. (f) Comparison between the TEM size distribution of the Ga$_2$O$_3$ NCs ($N(D)$) with the pore size distribution obtained from BJH ($V(D)/V^2$).
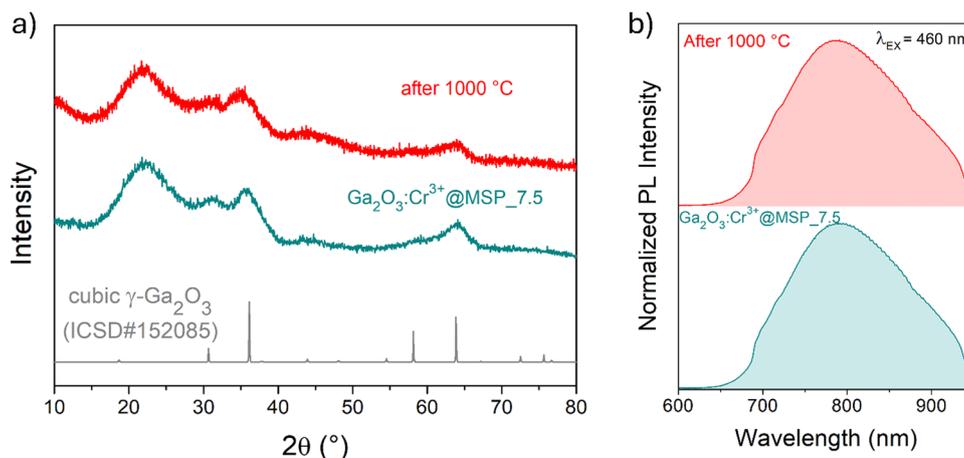
Fig. 5 Stability tests up to 1000 °C. (a) XRPD pattern of the sample before and after the TG−DSC analysis up to 1000 °C and (b) the corresponding normalized PL spectra obtained after excitation at 460 nm.

a broadband centered at about 792 nm and a FWHM of 2785 cm^{-1} due to the spin allowed ^{4}T$_2$ → ^{4}A$_2$ transition, typical of the weak crystal field materials, while the PLE spectrum is composed by the ^{4}A$_2$ → ^{4}T$_2$ and ^{4}A$_2$ → ^{4}T$_1$ transitions. It is well-known that to better understand the energy levels of transition metal ions in a crystal, the Tanabe–Sugano theory can be employed.[66] The crystal field strength 10Dq and the Racah parameters B and C can be directly estimated from the

excitation and emission band positions:

$$10Dq = E\left(^4A_2 \rightarrow {}^4T_2\right) \tag{1}$$

$$\frac{B}{Dq} = \frac{\left(\frac{\Delta E_{4_T}}{Dq}\right)^2 - 10\left(\frac{\Delta E_{4_T}}{Dq}\right)}{15\left(\frac{\Delta E_{4_T}}{Dq} - 8\right)} \tag{2}$$
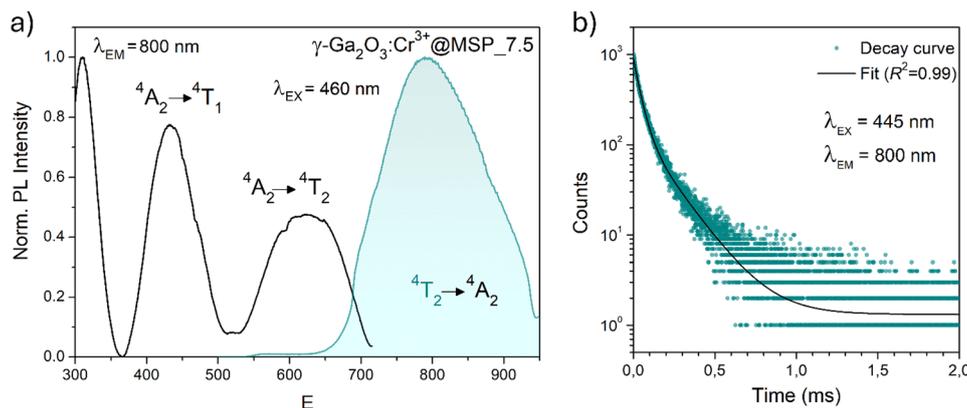
10934 | *J. Mater. Chem. C*, 2024, **12**, 10929–10941

This journal is © The Royal Society of Chemistry 2024

Fig. 6 PL and PLE spectra of the γ-Ga$_2$O$_3$:Cr^{3+}@MSP_7.5 sample after excitation at 460 nm and collecting at 800 nm, respectively. (b) Decay curve after excitation at 445 nm and collecting at 800 nm along with the fitting curve.

$$C \cong \frac{E(^2\mathrm{E})}{3.05} - \frac{7.90B}{3.05} + \frac{1.8}{3.08}\left(\frac{B^2}{Dq}\right) \quad (3)$$

where $\Delta E_{4\mathrm{T}} = E(^4\mathrm{T}_{1g}) - E(^4\mathrm{T}_{2g})$, the difference in energy between the $^4\mathrm{T}_{1g}$ and $^4\mathrm{T}_{2g}$ states. The energies of the $^4\mathrm{A}_2 \rightarrow {}^4\mathrm{T}_2$ and $^4\mathrm{A}_2 \rightarrow {}^4\mathrm{T}_1$ transition bands were estimated to be 15 873 cm^{-1} and 22 831 cm^{-1}, respectively. The 10Dq and B parameters are therefore calculated to be 15 873 cm^{-1} and 720 cm^{-1}, respectively, leading to a Dq/B of 2.2. This value is typical of the weak crystal field and smaller than the corresponding values for the rhombohedral α-Ga$_2$O$_3$:Cr^{3+} (2.97[15]) and monoclinic β-Ga$_2$O$_3$:Cr^{3+} (2.58[15]). In addition, a Stokes shift E_{Stokes} of 3247 cm^{-1} is estimated.

The PL decay curve of the spin-allowed $^4\mathrm{T}_2 \rightarrow {}^4\mathrm{A}_2$ transition of the γ-Ga$_2$O$_3$:Cr^{3+} NCs evidences a double-exponential behavior (fitted by $I(t) = I_0 + A_1\mathrm{e}^{-\frac{t}{\tau_1}} + A_2\mathrm{e}^{-\frac{t}{\tau_2}}$, where τ_i and A_i are the decay times and the corresponding amplitudes of the decay components) with an average decay time $\tau_{\mathrm{ave}} = (A_1\tau_1^2 + A_2\tau_2^2)/(A_1\tau_1 + A_2\tau_2)$ of 40 μs. The behaviour of the decay curve may be explained by considering the difference between the crystallographic sites in the core and the surface of the spinel NCs. In fact, for many oxide nanocrystals, it has been demonstrated that decreasing the size leads to a negative pressure at the surface, resulting in a deformation of the unit cell with a relative expansion with respect to the "bulk" core (e.g. MgO, CeO$_2$, Co$_3$O$_4$, Fe$_3$O$_4$, Cu$_2$O, Y$_2$O$_3$ and BaTiO$_3$[67-71]); stronger bonding at the core and a relaxation at the surface.[71,72] Therefore, Cr^{3+} ions could be stabilized in two slightly different octahedral sites of the same γ-phase, at the core and the surface of the NCs, reflecting the bi-exponential behaviour of the decay curve. However, the lifetime estimated is consistent with the conventional microsecond lifetimes of the $^4\mathrm{T}_2$ excited state of Cr^{3+} ions. It is worth noting that recently, Zhao et al. reported a persistent luminescence behaviour in γ-Ga$_2$O$_3$:Cr^{3+} by co-doping with Ba^{2+}.[73]

To fairly compare the effect of the environment of different compounds on the Cr^{3+} electrons, the Tanabe–Sugano diagram calculated for a specific C/B should be considered. To calculate the Racah parameter C, the $^2\mathrm{E}$ transition is necessary. However,

it is not clearly visible in the RT spectra. The low temperature PL spectrum was measured at 16 K (Fig. 7a). The peaks at 14 500 cm^{-1} and 14 365 cm^{-1} were assigned to the $^4\mathrm{T}_2$ zero phonon line (ZPL) and the $^2\mathrm{E}$, respectively (Fig. 7b). With the R-line value, the C parameter was calculated to be 3035 cm^{-1} and $C/B = 4.21$. Fig. 7c shows the Tanabe–Sugano diagram calculated for the specific C/B value.

Fig. S9 (ESI†) shows a comparison of the PL and PLE spectra of Cr^{3+} in the γ-Ga$_2$O$_3$, β-Ga$_2$O$_3$ and α-Ga$_2$O$_3$ polymorphs, while Table 1 summarizes the main parameters estimated.

By considering the γ-Ga$_2$O$_3$ spinel structure characterized by the cubic $Fd\bar{3}mZ$ space group reported by Zinkevich et al.[36] (ICDS#152085), a single GaO$_6$ octahedral site with an average $\langle$Ga–O$\rangle$ bond length of 2.0595 Å is present. The trends of the Dq/B parameter along with the Racah parameters B and C and therefore C/B can be explained taking into account the difference in the average $\langle$Ga–O$\rangle$ bond length of the octahedral site of the polymorphs. The weaker the bond (larger average $\langle$Ga–O$\rangle$) the larger the parameter B and the smaller Dq/B and C/B.

The temperature dependence of the PL spectra was investigated in the 16–500 K range (Fig. 8a). The integrated PL intensity as a function of temperature cannot be reproduced by the simple crossover quenching process described by the Struck and Fonger model.[74] As for the case of Eu^{2+}-[75,76] or Bi^{3+}-doped[77] phosphors, a double quenching barrier model is employed:

$$I(T) = \frac{I_0}{1 + A_1 \exp\left(-\frac{\Delta E_1}{k_\mathrm{B}T}\right) + A_2 \exp\left(-\frac{\Delta E_2}{k_\mathrm{B}T}\right)} \quad (4)$$

where I is the PL intensity, $A_i = \Gamma_{0,i}/\Gamma_{\nu,i}$ with $\Gamma_{\nu,i}$ the radiative rate and $\Gamma_{0,i}$ is the attempt rate of the nonradiative process, ΔE_i is the activation energy of the quenching processes, k_B is the Boltzmann constant and T is the temperature.

The two energy barriers can be associated with $^2\mathrm{E} \rightarrow {}^4\mathrm{A}_2$ (ΔE_1) and $^4\mathrm{T}_2 \rightarrow {}^4\mathrm{A}_2$ (ΔE_2) thermal quenching at lower and higher temperatures, respectively. From the fitting curve, the ΔE_1 activation energy was estimated to be 83 $\pm$ 11 cm^{-1}, in agreement with the small energy difference between the $^2\mathrm{E}$ and

This journal is © The Royal Society of Chemistry 2024
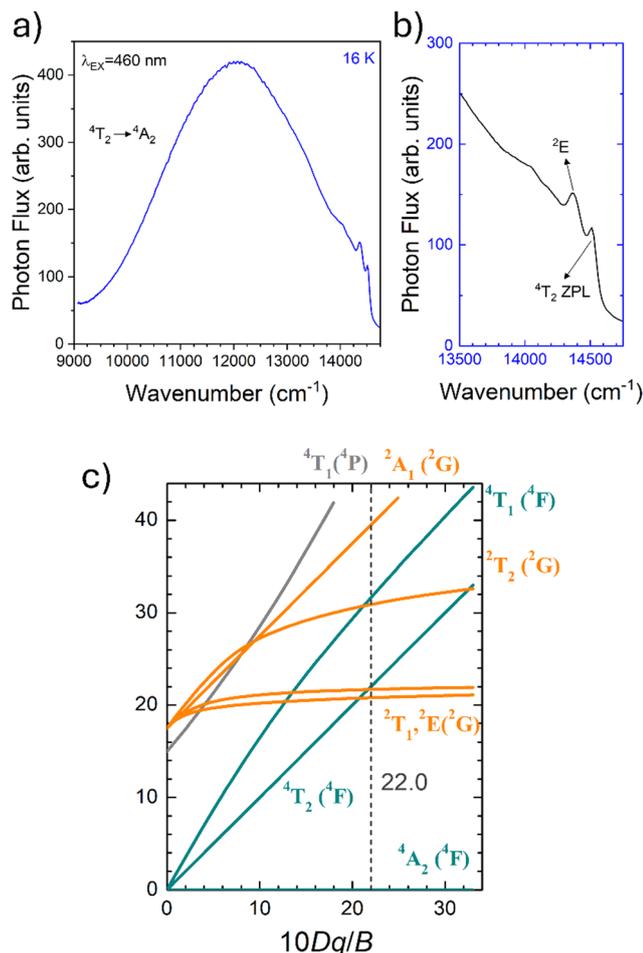
J. Mater. Chem. C, 2024, **12**, 10929–10941 | **10935**

Fig. 7 (a) The PL spectrum at 80 K collected at 800 nm and (b) magnification of the (A) $^4T_2$ zero phonon line and ^2E peaks, in the energy scale. (c) Tanabe–Sugano diagram calculated for Cr^{3+} in γ-Ga$_2$O$_3$ calculated considering C/B of 4.21.

the $^4T_2$ ZPL ($\sim$135 cm^{-1}) evidenced in Fig. 8b. On the other hand, a value of 1590 $\pm$ 63 cm^{-1} was estimated for the ΔE_2 activation energy related to the $^4T_2 \rightarrow {}^4A_2$ thermal quenching.

In addition, the temperature at which the intensity of the $^4T_2 \rightarrow {}^4A_2$ transition becomes 50% of that at low temperature, T_{50}, is estimated to be 415 K. Comparing this value with those estimated for the α-Ga$_2$O$_3$:Cr^{3+} (580 K[15]) and β-Ga$_2$O$_3$:Cr^{3+} (480 K[15]) polymorphs, a clear trend is evidenced. Indeed, the larger the average $\langle Ga–O \rangle$ bond length of the octahedral site, the lower the T_{50}.

The energetic distance $\Delta E'$ between $^4T_2$ and ^2E electronic manifolds obtained for a fixed position of ligand ions at the minimum energy of the ^2E parabola can be calculated as the

sum of the energy difference ΔE between the minimum energy of the $^4T_2$ and ^2E states and the $S\hbar\omega = E_{Stokes}/2$ energy: $\Delta E' = E_T^0 - E_E^0 = \Delta E + S\hbar\omega$.[78] By considering this lattice relaxation energy $S\hbar\omega$, in the framework of the perturbation approach and adiabatic approximation,[9,78] the configurational coordinate diagram is depicted in Fig. 8c by describing the ground state $^4A_2$ and the excited states ^2E and $^4T_2$ as single parabolic potential curves[79]

$$E_A(Q) = \frac{Q^2}{2} \tag{5}$$

$$E_E(Q) = \frac{Q^2}{2} + E_E^0 \tag{6}$$

$$E_T(Q) = \frac{Q^2}{2} - \sqrt{2S\hbar\omega}Q + E_T^0 \tag{7}$$

where Q represents the configurational coordinate (distance between Cr^{3+} and oxygen ions).

The configurational coordinate diagram confirms the very close position between the ^2E and the $^4T_2$ states, in agreement with the Tanabe–Sugano diagram. In addition, the PL spectral features of Cr^{3+} in the three polymorphs shown in Fig. S9 (ESI†) can be explained through the effect of the crystal field on the 3d^3 electrons of Cr^{3+}: the weaker crystal field in γ-Ga$_2$O$_3$ (Dq/B = 2.20) leads to the emission only from $^4T_2$, while the intermediate crystal field in β-Ga$_2$O$_3$ (Dq/B = 2.58) and the stronger field in α-Ga$_2$O$_3$ (Dq/B = 2.97) lead to emissions from both the $^4T_2$ and ^2E states, with a relative increase in the spin-forbidden $^2E \rightarrow {}^4A_2$ sharp line with respect to the spin-allowed $^4T_2 \rightarrow {}^4A_2$ broadband as the crystal field increases. This trend can also be understood by considering the average $\langle Ga–O \rangle$ bond length of the octahedral GaO$_6$ sites in the three polymorphs reported in Table 1 (the larger the average $\langle Ga–O \rangle$, the smaller the Dq/B), in agreement with the multiplet energy level diagram as a function of Cr–O bond length calculated by Ogasawara et al.[80] However, while the shift to a weaker crystal field in the Ga$_2$O$_3$ polymorphs leads to a red shift in the spin-allowed $^4T_2 \rightarrow {}^4A_2$ transition, its thermal quenching becomes more severe, being characterized by a smaller T_{50}.

Conclusions

In conclusion, this study has investigated the stabilization of Cr^{3+}-doped γ-Ga$_2$O$_3$ NCs within mesoporous silica particles of various pore sizes. Through comprehensive physical–chemical analyses including XRPD, SEM/HR-TEM, N$_2$ physisorption, and TG–DSC, the effects of size and temperature on the stabilization process were thoroughly examined. Spectroscopic

Table 1 Comparison of the 10Dq, B, C, Dq/B, C/B, $\langle Ga–O \rangle$ and T_{50} parameters for the different α-, β- and γ-Ga$_2$O$_3$:Cr^{3+} polymorphs

Phase	10Dq (cm^{-1})	B (cm^{-1})	C (cm^{-1})	Dq/B	C/B	$\langle Ga–O \rangle$ (Å)	T_{50} (K)	Ref.
γ	15 873	720	3035	2.20	4.21	2.059	415	This work
β	16 529	641	3187	2.58	4.97	2.012	480	15
α	16 393	552	3382	2.97	6.13	1.999	580	15

10936 | J. Mater. Chem. C, 2024, **12**, 10929–10941

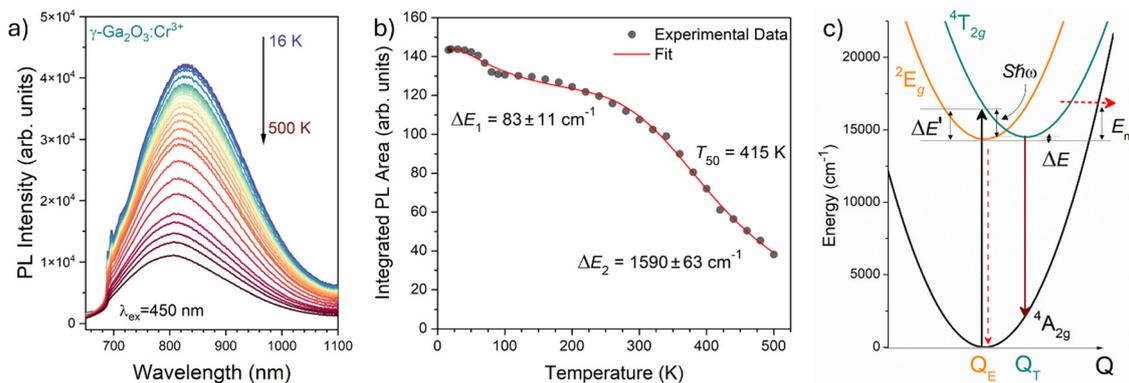This journal is © The Royal Society of Chemistry 2024

Fig. 8 (a) Temperature dependence of the PL emission spectra of γ-Ga$_2$O$_3$:Cr^{3+} NCs from 16 to 500 K (T). (b) Temperature dependence of the integrated PL intensity (black dots) and fit (red curve). (c) Configurational coordinate diagram constructed by using eqn (5)–(7).

analyses further elucidated the crystalline structure, confirming the stabilization of the cubic γ-Ga$_2$O$_3$ spinel structure. Moreover, detailed investigations of PL and PLE spectra, alongside temperature dependence studies in the 16–500 K range, provided valuable insights into the spectroscopic characteristics of Cr^{3+} within the γ-Ga$_2$O$_3$ matrix in the framework of Tanabe–Sugano theory, allowing the design of the configurational coordinate diagram. A comparison of the properties with respect to the β- and α-Ga$_2$O$_3$ polymorphs is provided. Importantly, the use of mesoporous silica particles as nanoreactors effectively stabilized the γ-Ga$_2$O$_3$:Cr^{3+} NCs, inhibiting the conventional phase transition to the β-phase up to 1000 °C, thus enhancing the stability of the γ-Ga$_2$O$_3$ phase.

Experimental

Materials

Chromium nitrate nonahydrate (Cr(NO$_3$)$_3$·9H$_2$O, 99%), cetyltrimethylammonium bromide (C$_{16}$H$_{33}$N(CH$_3$)$_3$Br, ≥98%), tetraethyl orthosilicate (Si(OC$_2$H$_5$)$_4$, 98%), ethanol (EtOH, ≥99.97%), methanol (MeOH, ≥99.9%), n-hexane (C$_6$H$_{12}$, ≥99%), Pluronic P-123 and 1,3,5-trimethylbenzene (C$_9$H$_{12}$, 98%) were purchased from Sigma-Aldrich. Ammonium hydroxide (NH$_4$OH, 28–30%) and sodium hydroxide (NaOH, 98%) were purchased from Applichem and gallium nitrate hydrate (Ga(NO$_3$)$_3$·xH$_2$O, 98.9%) from Alfa Aesar.

All the chemicals were of reagent grade and used without further purification.

Synthesis of MSPs of different pore sizes

MSPs characterized by an average pore size of 3.1 nm (MSP_3.1) were synthesized following the original work reported by Quiao et $al.$[47] The MSNs were synthesized in a flask thermostated at 60 °C using an ionic surfactant for the formation of micelles. 145.2 mL of milliQ water, 5.73 g of cetyltrimethylammonium bromide (CTABr) and 22.8 mL of ethanol are dissolved under vigorous stirring; then 1.25 mL of ammonium hydroxide are added. After about 30 minutes of waiting, 14.6 mL of tetraethoxysilane (TEOS) are added with sustained dripping, then all is left to react for two hours, always with vigorous stirring. Once

the synthesis is completed, the MSNs undergo centrifugal deposition cycles at 9000 rpm, elimination of solvent, washing and redispersion by ultrasound in milliQ water until total neutralization of pH. The last washing is carried out in ethanol. After washing, they are placed in an oven at 60 °C overnight to evaporate all the solvent, then they are ground in a mortar and calcined at 550 °C, with a rate of 2 °C min^{-1} for 6 hours.

To prepare MSPs with pores a little larger (MSP_4.2), the procedure described by Ma et $al.$[81] was followed. After solubilization of 0.8 g of CTABr and 3 mL of NaOH 2M in 400 mL of MilliQ water at room temperature, 60 mL of the swelling agent n-hexane was added. After 15 minutes of stirring, the mixture was stopped; then, 4 mL of TEOS were added after separation of the phases. The mixture was stirred again for 5 hours, filtered, washed several times with MeOH and dried at 60 °C overnight. MSNs were then ground in a mortar and calcined at 550 °C, with a rate of 2 °C min^{-1} for 5 hours.

SBA-15 MSPs with different pore size (MSP_7.5, MSP_13.5 and MSP_22.4) were synthesized following the procedures described in Zhao et $al.$[61,82] and Cao.[83] This synthesis was carried out in a 250 mL jacketed flask thermostat at 35 °C. The preparation takes place by dissolving 4 g of Pluronic P123 block copolymer (polyethylene oxide (EO) – polypropylene oxide (PO) – polyethylene oxide (EO) of formula EO20PO70EO20) in 30 mL of milliQ water and 116.5 mL of HCl 2M. At this point, for MSP_13.5 and MSP_22.4, the swelling agent trimethylbenzene (TMB) was added in 0.3 : 1 and 0.5 : 1 w/w ratios, respectively. After 30 minutes, 9 mL of TEOS were added with sustained dripping; then the whole mixture was left to react for 20 hours. The suspension was then placed in hermetically sealed Teflon containers in autoclaves for an aging process in an oven at 100 °C for 24 hours. After cooling to room temperature, the MSNs were washed with deionized water until the pH was neutralized. The last washing was carried out in ethanol. They were then placed in an oven at 100 °C for 6 hours in order to evaporate all the solvent and then calcined in a muffle furnace at 550 °C.

Impregnation method and γ-Ga$_2$O$_3$:Cr^{3+} NC formation

The precipitation of Ga$_2$O$_3$:Cr^{3+} NCs into the MSP mesopores was conducted by incipient wetness impregnation at room

temperature. The bare MSNs were dispersed in H_2O, keeping the mixture under stirring. After 30 minutes, the aqueous solutions of the precursor nitrate salts were added at the appropriate amount to the dispersion with continuous stirring for 2 h. The powder was recovered through the removal of the solvent by means of a rotary evaporator and treated at 900 °C for 2 h.

Silica etching

Silica etching was performed by placing the samples under stirring in a 2M NaOH solution for 2 h. After precipitation, the solvent was eliminated and the Ga_2O_3:Cr^{3+} NCs were dried at 60 °C overnight.

Bulk α-Ga_2O_3:Cr^{3+} and β-Ga_2O_3:Cr^{3+} references

Gallium nitrate and chromium nitrate solutions were prepared using $Ga(NO_3)_3 \cdot nH_2O$ (n = 7–9) (99.9%) and $Cr(NO_3)_3 \cdot 9H_2O$ (99.9%). The gallium and chromium solutions were stoichiometrically mixed to obtain $Ga_{0.998}Cr_{0.002}O_3$. In order to precipitate the hydroxide, ammonia solution (28%) was dropped into the mixed solution until the pH reached 6, and then kept stirring for 1 h. The obtained precipitate was separated using a centrifuge and washed with water. The washed product was dried at 100 °C for 2 days and the dried powder was finally treated at 500 °C for 12 h and at 1000 °C for 2 h to obtain α-Ga_2O_3:Cr^{3+} and β-Ga_2O_3:Cr^{3+}, respectively.

Characterization

Structural and morphological analysis

XRPD measurements at high angles were performed by means of a Philips diffractometer with a PW 1319 goniometer with Bragg–Brentano geometry, equipped with a focusing graphite monochromator and a proportional counter with a pulse-height discriminator. Nickel-filtered Cu Kα radiation and a step-by-step technique were employed (steps of 0.05° in 2θ), with a collection time of 30 s per step. XRPD measurements at low angles were performed by means of an Empyrean Series 3 (Malvern Panalytical) diffractometer equipped with a Cu anode X-ray tube, Bragg–Brentano HD incident-beam optic, and PIX-cel[3D] detector.

Size and morphology determination of the nanoparticles and EDS analysis were carried out with a Carl Zeiss Sigma VP Field Emission Scanning Electron Microscope (FE-SEM) equipped with a Bruker Quantax 200 microanalysis detector, with an accelerating voltage from 5 to 20 kV.

The TEM images were taken at 300 kV with a JEOL 3010 instrument with an ultrahigh resolution (UHR) pole-piece (0.17 nm point resolution), equipped with a Gatan slow-scan CCD camera (model 794) and an Oxford Instrument EDS microanalysis detector (model 6636). The powdered samples were dispersed in isopropyl alcohol solution by sonication and then deposited onto a holey carbon film.

Nitrogen adsorption–desorption isotherms were collected at liquid nitrogen temperature using a Micrometrics ASAP 2010

system. Each sample was degassed at 130 °C overnight before the measurements. The Brunauer–Emmett–Teller (BET) equation was used to calculate the specific surface area from the adsorption data and the Barrett–Joyner–Halenda (BJH) model was used to estimate the pore-size distribution from the adsorption branches of the isotherms.

The determination of gallium (Ga) and chromium (Cr) concentrations was conducted using Inductively Coupled Plasma Optical Emission Spectrometry (ICP-OES). In the procedure, approximately 10 mg of the sample was transferred into a 50 mL polypropylene (PP) tube. The sample was then subjected to mineralization with 20 mL of aqua regia (a mixture of ultra-pure hydrochloric acid and nitric acid in a 3 : 1 volume ratio) through sonication for 2 hours at 25 °C, using a frequency of 40 kHz at 80% intensity (CP104 model from CEIA, Arezzo). This step was followed by mechanical stirring overnight at 100 rpm (VDRL 711 Opto-lab, Modena). Subsequently, the mineralized sample was diluted to a final volume of 50 mL using Milli-Q water (with a resistivity of 18 MΩ cm) and stored at 4 °C. Prior to analysis, the sample was further diluted twofold with Milli-Q water. Alongside the samples, a procedural blank was also prepared for comparison. The analysis itself was performed on an iCAP 7000 Plus instrument (Thermo Scientific, Bremen), which is equipped with a glass concentric nebulizer and a cyclonic spray chamber made of glass. The detection of Ga and Cr was executed in axial mode, targeting their emission lines at 283.563 nm and 294.364 nm, respectively. Quantification of these elements was achieved through external calibration using mono-elemental standard solutions (provided by UltraScientific, Milan). Five replicates of blanks, standards, and sample measurements were taken and averaged.

Thermogravimetric analysis (TGA) and differential scanning calorimetry (DSC) have been performed with a Netzsch STA 409C in air from 30 to 1000 °C at a heating rate of 10 °C min^{-1}. The instrument was purged with a mixture of air and N_2 at a 40 mL min^{-1} flow rate. The analysis was performed with an alumina crucible for compatibility. Alumina was used for internal calibration. Three replicates were performed for each sample. Data were collected with STA Netzsch software.

Spectroscopic measurements and temperature-dependent photoluminescence

PL emission and PLE excitation spectra were obtained using a Horiba–Jobin Yvon Fluorolog 3–21 spectrofluorometer. The photoluminescence spectra were collected by exciting the samples by means of a xenon arc lamp (450 W), selecting the excitation wavelength using a double Czerny–Turner monochromator and collecting with a R928 PMT (Hamamatsu) and a QEPro-XR (Ocean Insight). All spectra were recorded at RT under the same conditions.

Time-resolved PL measurements were carried out under excitation at 445 nm using a pulsed SpectraLED (Horiba Scientific) through the Fluorolog-Time Correlated Single Photon Counting system.

The temperature dependence of PL spectra (16–500 K) was investigated with a cryostat (Janis ST-500, Lake Shore

10938 | J. Mater. Chem. C, 2024, 12, 10929–10941

This journal is © The Royal Society of Chemistry 2024

Cryotronics., Inc.), exciting with a 450 nm LD and collecting using a Hamamatsu PMA-12 CCD (C10027-02). All the spectra were calibrated using a standard halogen lamp (DH-2000CAL, Ocean Optics) to obtain spectra in the photon flux scale. In addition, the photon flux per constant wavelength interval function, $\phi(\lambda)$, is converted to photon flux per energy interval by using the Jacobian transformation.

Author contributions

All authors discussed and contributed to the interpretation of the results and the final manuscript. M. B. conceived the presented idea. M. B., J. X., P. R. and A. B. planned the experiments. M. C., M. B. and A. S. prepared the samples. M. B., M. C., C. B., J. X., T. N., J. U., F. D., E. B. and D. C. carried out the experiments. M. B. supervised the project. A. B., S. T., T. N. and F. R. helped supervise the project. M. B. wrote the manuscript with support from M. C., P. R. and A. B.

Data availability

The data supporting this article are provided in the ESI.†

Conflicts of interest

There are no conflicts to declare.

Acknowledgements

Notes and references

1 T. H. Maiman, *Nature*, 1960, **187**, 493–494.
2 T. Maldiney, A. Bessiere, J. Seguin, E. Teston, S. K. Sharma, B. Viana, A. J. J. Bos, P. Dorenbos, M. Bessodes, D. Gourier, D. Scherman and C. Richard, *Nat. Mater.*, 2014, **13**, 418–426.
3 A. Bessiere, S. K. Sharma, N. Basavaraju, K. R. Priolkar, L. Binet, B. Viana, A. J. J. Bos, T. Maldiney, C. Richard, D. Scherman and D. Gourier, *Chem. Mater.*, 2014, **26**, 1365–1373.
4 J. Ueda, P. Dorenbos, A. J. J. Bos, K. Kuroishi and S. Tanabe, *J. Mater. Chem. C*, 2015, **3**, 5642–5651.
5 Y. Zhuang, Y. Katayama, J. Ueda and S. Tanabe, *Opt. Mater.*, 2014, **36**, 1907–1912.
6 J. Xu, J. Ueda, Y. Zhuang, B. Viana and S. Tanabe, *Appl. Phys. Express*, 2015, **8**, 042602.
7 Y. Katayama, H. Kobayashi and S. Tanabe, *Appl. Phys. Express*, 2015, **8**, 012102.
8 M. Back, E. Trave, J. Ueda and S. Tanabe, *Chem. Mater.*, 2016, **28**, 8347–8356.
9 M. Back, J. Ueda, M. G. Brik, T. Lesniewski, M. Grinberg and S. Tanabe, *ACS Appl. Mater. Interfaces*, 2018, **10**, 41512–41524.
10 M. Back, J. Ueda, J. Xu, K. Asami, M. G. Brik and S. Tanabe, *Adv. Opt. Mater.*, 2020, **8**, 2000124.
11 A. Kabanski, M. Ptak and D. Stefanska, *ACS Appl. Mater. Interfaces*, 2023, **15**, 7074–7082.
12 Z. Ristic, V. Dordevic, M. Medic, S. Kuzman, M. G. Brik, Z. Antic and M. D. Dramicanin, *Opt. Mater.*, 2021, **120**, 111486.
13 M. Back, J. Ueda, M. G. Brik and S. Tanabe, *ACS Appl. Mater. Interfaces*, 2020, **12**, 38325–38332.
14 J. Ueda, M. Back, M. G. Brik, Y. Zhuang, M. Grinberg and S. Tanabe, *Opt. Mater.*, 2018, **85**, 510–516.
15 M. Back, J. Ueda, H. Nambu, M. Fujita, A. Yamamoto, H. Yoshida, H. Tanaka, M. G. Brik and S. Tanabe, *Adv. Opt. Mater.*, 2021, **9**, 2100033.
16 R. A. Forman, G. J. Piermarini, J. D. Barnett and S. Block, *Science*, 1972, **176**, 284–285.
17 G. J. Piermarini, S. Block, J. D. Barnett and R. A. Forman, *J. Appl. Phys.*, 1975, **46**, 2774–2780.
18 H. K. Mao, P. M. Bell, J. W. Shaner and D. J. Steinberg, *J. Appl. Phys.*, 1978, **49**, 3276–3283.
19 M. Back, J. Ueda, H. Hua and S. Tanabe, *Chem. Mater.*, 2021, **33**, 3379–3385.
20 M. Szymczak, P. Wozny, M. Runowski, M. Pieprz, V. Lavin and L. Marciniak, *Chem. Eng. J.*, 2023, **453**, 139632.
21 I. Widmann, G. Kinik, M. Jahnig, R. Glaum, M. Schwarz, C. Wustefeld, D. Johrendt, M. Tribus, C. Hejny, L. Bayarjargal, L. Dubrovinsky, G. Heymann, M. Suta and H. Huppertz, *Adv. Funct. Mater.*, 2024, 2400054.
22 R.-J. Xie, *Light: Sci. Appl.*, 2020, **9**, 155.
23 M. Mao, T. Zhou, H. Zeng, L. Wang, F. Huang, X. Tang and R.-J. Xie, *J. Mater. Chem. C*, 2020, **8**, 1981–1988.
24 G. N. A. De Guzman, M.-H. Fang, C.-H. Liang, Z. Bao, S.-F. Hu and R.-S. Liu, *J. Lumin.*, 2020, **219**, 116944.
25 S. J. Pearton, J. Yang, P. H. CaryIV, F. Ren, J. Kim, M. J. Tadjer and M. A. A. Mastro, *Appl. Phys. Rev.*, 2018, **5**, 011301.
26 R. Roy, V. G. Hill and E. F. Osburn, *J. Am. Chem. Soc.*, 1952, **74**, 719.
27 H. H. Tippins, *Phys. Rev.*, 1965, **137**, A865.
28 D. Vivien, B. Viana, A. Revcolevschi, J. D. Barrie, P. Nelson and O. M. Stafsudd, *J. Lumin.*, 1987, **39**, 29.
29 C. G. Walsh, J. F. Donegan, T. J. Glynn, G. P. Morgan, G. F. Imbusch and J. P. Remeika, *J. Lumin.*, 1988, **40–41**, 103.
30 Y. Tokida and S. Adachi, *J. Appl. Phys.*, 2012, **112**, 063522.
31 A. Segure, L. Artus, R. Cuscó, R. Goldhahn and M. Feneberg, *Phys. Rev. Mater.*, 2017, **1**, 024604.

This journal is © The Royal Society of Chemistry 2024

J. Mater. Chem. C, 2024, **12**, 10929–10941 | **10939**

32 M.-H. Fang, G. N. A. De Guzman, Z. Bao, N. Majewska, S. Mahlik, M. Grinberg, G. Leniec, S. M. Kaczmarek, C.-W. Yang, K.-M. Lu, H.-S. Sheu, S.-F. Hu and R.-S. Liu, *J. Mater. Chem. C*, 2020, **8**, 11013–11017.

33 H. Yusa and M. Miyakawa, *Inorg. Chem.*, 2024, **63**, 2695–2700.

34 M.-H. Fang, K.-C. Chen, N. Majewska, T. Lesniewski, S. Mahlik, G. Leniec, S. M. Kaczmarek, C.-W. Yang, K.-M. Lu, H.-S. Sheu and R.-S. Liu, *ACS Energy Lett.*, 2021, **6**, 109–114.

35 K.-C. Chen, M.-H. Fang, W.-T. Huang, M. Kaminski, N. Majewska, T. Lesniewski, S. Mahlik, G. Leniec, S. M. Kaczmarek, C.-W. Yang, K.-M. Lu, H.-S. Sheu and R.-S. Liu, *Chem. Mater.*, 2021, **33**, 3832–3840.

36 M. Zinkevich, F. M. Morales, H. Nitsche, M. Ahrens, M. Ruehle and F. Aldiger, *Z. Metallkd.*, 2004, **95**, 756–762.

37 H. Y. Playford, A. C. Hannon, E. R. Barney and R. I. Walton, *Chem. – Eur. J.*, 2013, **19**, 2803–2813.

38 H. Y. Playford, A. C. Hannon, M. G. Tucker, D. M. Dawson, S. E. Ashbrook, R. J. Kastiban, J. Sloan and R. I. Walton, *J. Phys. Chem. C*, 2014, **118**, 16188–16198.

39 P. Castro-Fernandez, M. V. Blanco, R. Verel, E. Willinger, A. Fedorov, P. M. Abdala and C. R. Müller, *J. Phys. Chem. C*, 2020, **124**, 20578–20588.

40 L. E. Ratcliff, T. Oshima, F. Nippert, B. M. Janzen, E. Kluth, R. Goldhahn, M. Feneberg, P. Mazzolini, O. Bierwagen and C. Wouters, *et al.*, *Adv. Mater.*, 2022, **34**, 2204217.

41 N. V. Golubev, E. S. Ignat'eva, V. N. Sigaev, A. Lauria, L. De Trizio, A. Azarbod, A. Paleari and R. Lorenzi, *Phys. Chem. Chem. Phys.*, 2015, **17**, 5141–5150.

42 R. Lorenzi, N. V. Golubev, E. S. Ignat'eva, V. N. Sigaev, C. Ferrara, M. Acciarri, G. M. Vanacore and A. Paleari, *J. Colloid Interface Sci.*, 2022, **608**, 2830–2838.

43 Z. Yang, L. X. Song, Y. Q. Wang, M. M. Ruan, Y. Teng, J. Xia, J. Yang, S. S. Chen and F. Wang, *J. Mater. Chem. A*, 2018, **6**, 2914–2921.

44 P. Castro-Fernandez, D. Mance, C. Liu, I. B. Moroz, P. M. Abdala, E. A. Pidko, C. Copéret, A. Fedorov and C. R. Müller, *ACS Catal.*, 2021, **11**, 907–924.

45 T. Wang, S. S. Farvid, M. Abulikemu and P. V. Radovanovic, *J. Am. Chem. Soc.*, 2010, **132**, 9250–9252.

46 T. Wang, V. Chirmanov, W. H. M. Chiu and P. V. Radovanovic, *J. Am. Chem. Soc.*, 2013, **135**, 14520–14523.

47 Z. A. Qiao, L. Zhang, M. Guo, Y. Liu and Q. Huo, *Chem. Mater.*, 2009, **21**, 3823–3829.

48 C. Xin, N. Zhao, H. Zhan, F. Xiao, W. Wie and Y. Sun, *J. Colloid Interface Sci.*, 2014, **433**, 176–182.

49 T. Lu, X. D. Yao, G. Q. Lu and Y. He, *J. Colloid Interface Sci.*, 2009, **336**, 368–373.

50 J. N. Israelachvili, *Intermolecular and Surface Forces*, Academic Press, London, 1985.

51 T. Shimizu, M. Masuda and H. Minamikawa, *Chem. Rev.*, 2005, **105**, 1401–1444.

52 Y. Yoshioka, H. Hayashi, A. Kuwabara, F. Oba, K. Matsunaga and I. Tanaka, *J. Phys.: Condens. Matter*, 2007, **19**, 346211.

53 J. Zhao, J. Byggmastar, H. He, K. Nordlund, F. Djurabekova and M. Hua, *npj Comput. Mater.*, 2023, **9**, 159.

54 C. B. Murray, D. J. Norris and M. G. Bawendi, *J. Am. Chem. Soc.*, 1993, **115**, 8706–8715.

55 D. V. Talapin, A. L. Rogach, A. Kornowski, M. Haase and H. Weller, *Nano Lett.*, 2001, **1**, 207–211.

56 R. C. Garvie, *J. Phys. Chem.*, 1965, **69**, 1238–1243.

57 P. Ayyub, V. R. Palkar, S. Chattopadhyay and M. Multani, *Phys. Rev. B: Condens. Matter Mater. Phys.*, 1995, **51**, 6135–6138.

58 M.-H. Fang, T.-Y. Li, W.-T. Huang, C.-L. Cheng, Z. Bao, N. Majewska, S. Mahlik, C.-W. Yang, K.-M. Lu, G. Leniec, S. M. Kaczmarek, H.-S. Sheu and R.-S. Liu, *ACS Energy Lett.*, 2021, **6**, 659–664.

59 J. Wang, X. Guan, H. Zheng, L. Zhao, R. Jiang, P. Zhao, Y. Zhang, J. Hu, P. Li, S. Jia and J. Wang, *Nano Lett.*, 2023, **23**, 7364–7370.

60 M. Thommes, K. Kaneko, A. V. Neimark, J. P. Olivier, F. Rodriguez-Reinoso, J. Rouquerol and K. S. W. Sing, *Pure Appl. Chem.*, 2015, **87**, 1051–1069.

61 D. Zhao, J. Feng, Q. Huo, N. Melosh, G. H. Fredrickson, B. F. Chmelka and G. D. Stucky, *Science*, 1998, **279**, 548–552.

62 M. Kruk, M. Jaroniec, C. H. Ko and R. Ryoo, *Chem. Mater.*, 2000, **12**, 1961–1968.

63 G. Sponchia, R. Marin, I. Freris, M. Marchiori, E. Moretti, L. Storaro, P. Canton, A. Lausi, A. Benedetti and P. Riello, *J. Nanopart. Res.*, 2014, **16**, 2245.

64 C. Wouters, M. Nofal, P. Mazzolini, J. Zhang, T. Remmele, A. Kwasniewski, O. Bierwagen and M. Albrecht, *APL Mater.*, 2024, **12**, 011110.

65 X. Zhang, H. Huang, Y. Zhang, D. Liu, N. Tong, J. Lin, L. Chen, Z. Zhang and X. Wang, *ACS Omega*, 2018, **3**, 14469–14476.

66 Y. Tanabe and S. Sugano, *J. Phys. Soc. Jpn.*, 1954, **9**, 766.

67 S.-W. Chan and W. Wang, *Mater. Chem. Phys.*, 2021, **273**, 125091.

68 V. Perebeinos, S.-W. Chan and F. Zhang, *Solid State Commun.*, 2002, **123**, 295–297.

69 G. Kimmel, A. Sahartov, Y. Sadia, Z. Porat, J. Zabicky and E. Dvir, *J. Mater. Res. Technol.*, 2021, **12**, 87–99.

70 C. Beck, K. H. Ehses, R. Hempelmann and C. Bruch, *Scr. Mater.*, 2001, **44**, 2127–2131.

71 M. Fukuhara, *Phys. Lett. A*, 2003, **313**, 427–430.

72 M. Leoni, *Mater. Sci. Forum*, 2004, **443–444**, 1–10.

73 T. Zhao, R. Abdurahman, Q. Yang, R. Aiwaili and X.-B. Yin, *J. Mater. Chem. C*, 2024, **12**, 498–507.

74 C. W. Struck and W. H. Fonger, *J. Appl. Phys.*, 1971, **42**, 4515–4516.

75 P. F. Smet, J. E. Van Haecke, F. Loncke, H. Vrielinck, F. Callens and D. Poelman, *Phys. Rev. B: Condens. Matter Mater. Phys.*, 2006, **74**, 035207.

76 S. Mahlik, K. Wisniewski, M. Grinberg and R. S. Meltzer, *J. Phys.: Condens. Matter*, 2009, **21**, 245601.

77 M. Back, J. Ueda, J. Xu, K. Asami, L. Amidani, E. Trave and S. Tanabe, *J. Phys. Chem. C*, 2019, **123**, 14677–14688.

78 M. Grinberg and A. Suchocki, *J. Lumin.*, 2007, **125**, 97–103.

79 M. Grinberg and T. Lesniewski, *J. Lumin.*, 2019, **214**, 116574.

10940 | *J. Mater. Chem. C*, 2024, **12**, 10929–10941

This journal is © The Royal Society of Chemistry 2024

80 K. Ogasawara, F. Alluqmani and H. Nagoshi, *ECS J. Solid State Sci. Technol.*, 2016, **5**, R3191.

81 S. Ma, Y. Wang and Y. Zhu, *J. Porous. Mater.*, 2011, **18**, 233–239.

82 D. Zhao, Q. Huo, J. Feng, B. F. Chmelka and G. D. Stucky, *J. Am. Chem. Soc.*, 1998, **120**, 6024–6036.

83 L. Cao, T. Man and M. Kruk, *Chem. Mater.*, 2009, **21**, 1144–1153.

This journal is © The Royal Society of Chemistry 2024

J. Mater. Chem. C, 2024, **12**, 10929–10941 | **10941**